Numerical simulation of the surface hardening of steel

Jürgen Fuhrmann and Dietmar Hömberg

Weierstrass Institute for Applied Analysis and Stochastics
Mohrenstraße 39
D – 10117 Berlin
Germany

Abstract

We discuss a model that is capable of describing the solid–solid phase transitions in steel. It consists of a system of ordinary differential equations for the volume fractions of the occuring phases coupled with a nonlinear energy balance equation to take care of the latent heats of the phase changes.

This model is applied to simulate surface heat treatments, which play an important role in the manufacturing of steel. Two different technologies are considered: laser and induction hardening. In the latter case the model has to be extended by Maxwell's equations.

Finally, we present numerical simulations of laser and surface hardening applied to the steel 42 CrMo 4.

Keywords: finite volume method, heat treatment, induction hardening, laser hardening, phase transitions.

1 Introduction

In most structural components in mechanical engineering, the surface is particularly stressed. Therefore, the aim of surface hardening is to increase the hardness of the boundary layers of a workpiece by rapid heating and subsequent quenching. This heat treatment leads to a change in microstructure, which produces the desired hardening effect. Typical examples of application are all sorts of cutting tools, (gear–) wheels, driving axles, to name only a few.

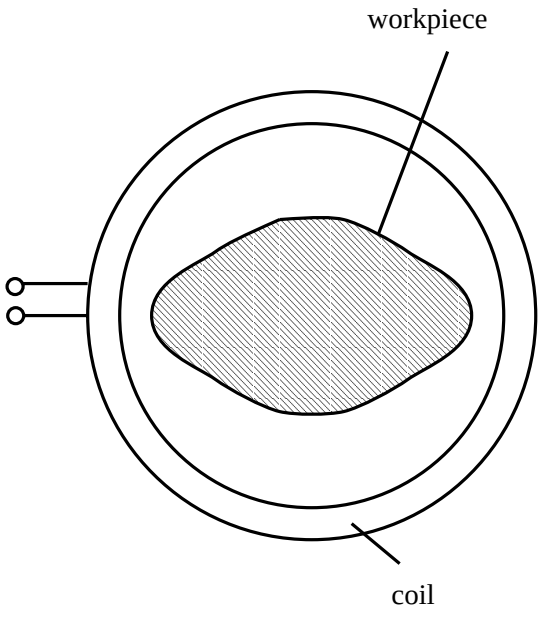

Figure 1: Sketch of an induction hardening facility.

In this paper we investigate two different methods for surface hardening: induction and laser hardening.
The mode of operation in induction hardening facilities relies on the transformer principle. A given current density in the coil induces eddy currents inside the workpiece Ω (cf. Fig. 1). Because of the Joule effect these eddy currents lead to an increase in temperature in the boundary layers of the workpiece. Then the current is switched off and the workpiece is quenched by spray–water cooling.
When the workpiece is very big or the part of the surface to be hardened has a complicated shape, laser hardening becomes attractive. In this process a laser beam moves along the surface of a workpiece (cf. Fig. 2). The laser radiation is absorbed by the workpiece, leading to a rapid heating of its boundary layers. Then, the workpiece is quenched by 'self–cooling' of the workpiece.

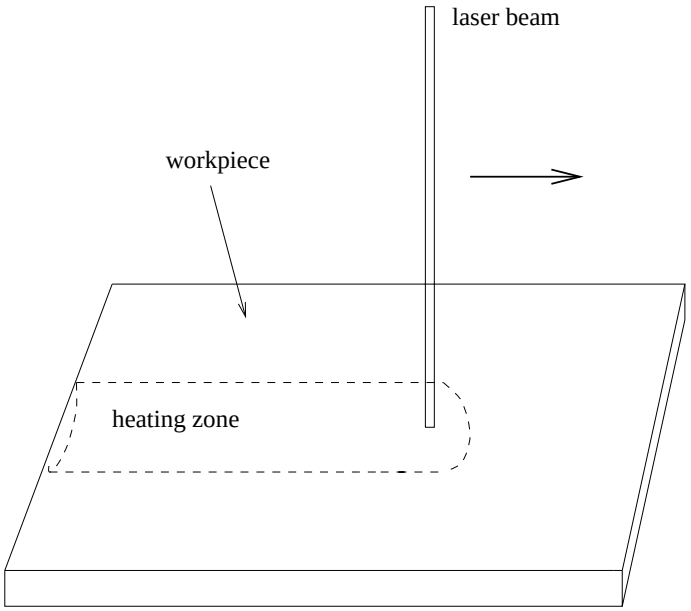

Figure 2: Sketch of a laser hardening process

To increase the scanning width, sometimes the laser beam performs an additional oscillating movement orthogonally to the principal moving direction.
In Section 2 we discuss a mathematical model to describe these heat treatments. Basic ingredients are a rate law to describe the evolution of the phase transitions, which are responsible for the change in hardness of the workpiece. To take care of recalescence effects, this is coupled with an energy balance equation. In addition we have to describe models for laser radiation and Joule heating, respectively. Section 3 is devoted to developing a numerical algorithm for surface heat treatments. Then, in Section 4 we present numerical simulations for both laser and induction hardening. Finally, in the last section we make some concluding remarks concerning model improvements and further directions

of research.

2 Model equations

2.1 The phase transitions

The reason why one can change the hardness of steel by thermal treatment lies in the occuring phase transitions, depicted in Fig. 3. At room temperature, in general, steel is a mixture of ferrite, pearlite, bainite and martensite. Upon heating, these phases are transformed to austenite. Then, during cooling austenite is transformed back to a mixture of ferrite, pearlite, bainite and martensite.
The actual phase distribution at the end of the heat treatment depends on the cooling strategy. In the case of surface hardening, owing to high cooling rates most of the austenite is transformed to martensite by a diffusionless phase transition leading to the desired increase of hardness.

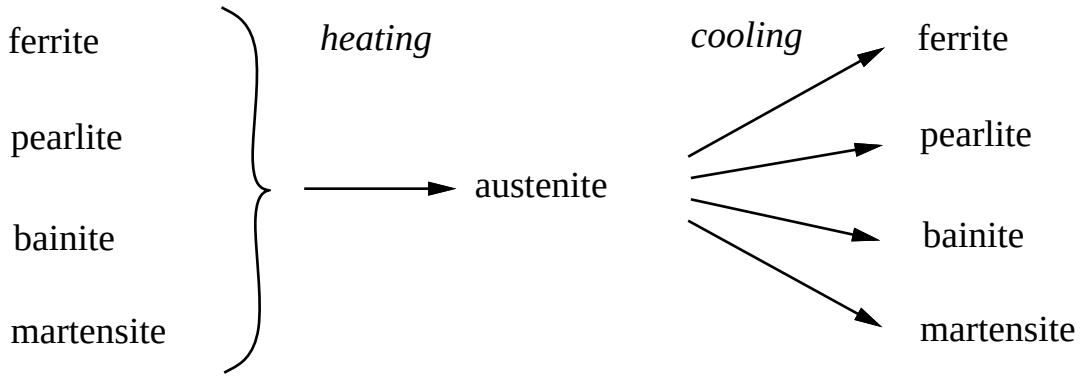

Figure 3: Possible phase transitions in steel

Mathematical models for phase transitions in steel have been considered e.g.in [8]–[11], [15], [19], [20]. For a survey on mathematical models for laser material treatments, we refer to [14].
Before presenting our model we recall some classical approaches for typical phase transitions.
The simplest way to describe diffusive phase transitions like the *austenite – pearlite transformation* in the isothermal case is the Johnson–Mehl equation

$$p(t) = 1 - e^{-c_1(\theta)t^{c_2(\theta)}}, \tag{2.1}$$

where p is the volume fraction of pearlite and c_1, c_2 are temperature–dependent coefficients, to be determined from *Time–Temperature–Transformation Diagrams* (cf. [10] for details).

In the nonisothermal case, a widely used approach is to apply *Scheil's additivity rule* (for details and further references we again refer to [10]):

$$\int_0^t \frac{1}{\tilde{\tau}(\theta(\xi), p(t))} d\xi = 1. \tag{2.2}$$

Here, $\tilde{\tau}(\theta, p)$ is the time to transform the fraction p to pearlite isothermally at temperature θ. Recently, Fasano and Primicerio [5] showed that only those functions $\tilde{\tau}$ are admissible for (2.2) that are separable, i.e. that have the form

$$\tilde{\tau}(\theta, p) = \tau_1(\theta) \cdot \tau_2(p). \tag{2.3}$$

Note that c_2 has to be constant, if one wants to utilize (2.1) to compute $\tilde{\tau}$.
In view of (2.3), it is easily seen that the additivity rule (2.2) is equivalent to a separable rate law

$$\begin{aligned} p(t_0) &= p_0, & \text{(2.4a)} \\ p_t(t) &= f_1(\theta(t)) f_2(p(t)). & \text{(2.4b)} \end{aligned}$$

The *austenite – martensite phase transition* is diffusionless and temperature dependent. Only during nonisothermal stages of a cooling process, an increase in the martensite fraction can be observed.
The easiest way to describe this behaviour is by the rate law

$$\begin{aligned} m(t_0) &= 0, & \text{(2.5a)} \\ m_t(t) &= (1 - m(t)) f_3(\theta) \mathcal{H}(-\theta_t), & \text{(2.5b)} \end{aligned}$$

where $\mathcal{H}$ is a smooth, monotone approximation of the Heaviside graph. Whenever the temperature is non–decreasing, $-\theta_t \geq 0$ and hence $m_t = 0$.
According to Leblond and Deveaux [15], the formation of *austenite* cannot be described by the additivity rule, since for fixed temperature within the transformation range, one can get an equilibrium volume fraction of austenite less than one. Therefore, they propose to use the rate law

$$\begin{aligned} a(t_0) &= 0, & \text{(2.6a)} \\ a_t(t) &= \frac{1}{\tau(\theta)} \max\left\{ \left(a_{eq}(\theta) - a(t) \right), 0 \right\}, & \text{(2.6b)} \end{aligned}$$

with an equilibrium fraction of austenite a_{eq} and a time–constant τ.

Remark 2.1 *(1) Originally, in [15] the formula*

$$a_t(t) = \frac{1}{\tau(\theta)}\Big(a_{eq}(\theta) - a(t)\Big)$$

was proposed. However, since we want to describe a complete heat treatment cycle, we had to make this modification to assure that (2.6b) only describes the growth and not the shrinking of austenite.

(2) If one wants to avoid the nonlinearity in θ_t, another way to describe the growth of martensite would be a formula similar to (2.6a–b).

To formulate a general model for phase transitions according to Fig. 3, we introduce the following notations:

z_0: volume fraction of austenite,

$z_1, ..., z_4$: relative volume fractions of ferrite, pearlite, bainite, martensite, which have been transformed from z_0,

A_s: critical temperature, above which the formation of austenite starts,

M_s: critical temperature, below which the formation of martensite starts ($M_s < A_s$).

We describe the evolution of volume fractions for given temperature evolution $\theta(.)$ by the following initial–value problem:

$$z_0(0) = z_{00} \in (0,1), \tag{2.7a}$$

$$z_i(0) = 0, \qquad i = 1, ..., 4, \tag{2.7b}$$

$$z_{0,t}(t) = \frac{1}{\tau(\theta)} \max\Big\{\Big(a_{eq}(\theta(t)) - z_0(t)\Big)\,,\, 0\Big\}\,\mathcal{H}(\theta(t) - A_s) - \sum_{j=1}^{4} z_{j,t}(t) \tag{2.7c}$$

$$z_{i,t}(t) = g_i(t, z(t), \theta(t))\,\mathcal{H}(A_s - \theta(t)), \qquad i = 1, ..., 3, \tag{2.7d}$$

$$z_{4,t}(t) = z_0(t)\mathcal{H}(-\theta_t) g_4(t, z(t), \theta(t))\,\mathcal{H}(M_s - \theta(t)), \tag{2.7e}$$

where we assume

(A1) $\mathcal{H} \in C^\infty(\mathbb{R})$, monotone regularization of the Heaviside graph, satisfying $\mathcal{H}(0) = 0$ (cf. [18], p. 196).

(A2) $a_{eq} \in C^{1,1}(\mathbb{R})$, $a_{eq}(x) \in [0,1]$ for all $x \in \mathbb{R}$.

(A3) $\tau \in C^{1,1}(\mathbb{R})$, $m \le \tau(x) \le M$ for all $x \in \mathbb{R}$, and constants $0 < m < M$,

(A4) $g_i \in C^{1,1}(D)$, $i = 1, \ldots, 4$, $D = [0,T] \times [0,1]^5 \times \mathbb{R}$, moreover

$0 \le g_i \le M$, for all $(t, z, \theta) \in D$ and a constant $M > 0$.

In Section 4 we will show how this general model can be utilized for the simulation of surface heat treatments.

2.2 Energy balance equation

Neglecting mechanical effects and using Fourier's law of heat conduction, we consider the following heat transfer equation:

$$\rho(\theta)c(\theta)\theta_t - \nabla.\Big(k(\theta)\nabla\theta\Big) = F_1(\theta,z) + F_2, \quad \text{in } Q_T = \Omega \times (0,T). \tag{2.8}$$

Here, $\Omega \subset \mathbb{R}^n$, $n = 2,3$ is the workpiece and ρ, c, k denote density, specific heat at constant pressure and heat conductivity, respectively. The terms F_1, F_2 will take care of the latent heats of the phase transitions and the heat source to be decribed in the following subsections.

We consider a Newton-type boundary condition

$$-k(\theta)\frac{\partial\theta}{\partial\nu} = \gamma(x,t)(\theta - \theta_\Gamma) \quad \text{in } \Sigma_T = \partial\Omega \times (0,T),$$

and the initial condition

$$\theta(.,0) = \theta_0 \quad \text{in } \Omega.$$

Let $L_i > 0$, $i = 0,\ldots,4$, be the amount of latent heat consumed or released during the phase transitions. Then, F_1 takes the form

$$F_1(\theta,z) = -F_{11}(\theta,z)A(\theta_t) + F_{12}(\theta,z),$$

with

$$\begin{aligned}
A(\theta_t) &= -\mathcal{H}(-\theta_t), && (2.9a)\\
F_{11}(\theta,z) &= \rho(\theta)L_4 g_4(t,z,\theta)\mathcal{H}(M_s - \theta), && (2.9b)\\
F_{12}(\theta,z) &= -\frac{\rho(\theta)L_0}{\tau(\theta)}\max\Big\{\Big(a_{eq}(\theta) - z_0\Big)\,,\,0\Big\}\,\mathcal{H}(\theta - A_s)\\
&\qquad +\rho(\theta)\sum_{i=1}^{3} L_i g_i(t,z,\theta)\,\mathcal{H}(A_s - \theta). && (2.9c)
\end{aligned}$$

Hence, in view of (2.7a-e) and (A1)–(A4), latent heat is consumed during the growth of austenite ($z_{0,t} \geq 0$) and released during the formation of ferrite, pearlite, bainite and martensite.

Inserting (2.9a-c) into (2.8), we obtain the following nonlinear energy balance equation:

$$\begin{aligned}
\rho(\theta)c(\theta)\theta_t + F_{11}(\theta,z)A(\theta_t) - \nabla.\Big(k(\theta)\nabla\theta\Big) &= F_{12}(\theta,z) + F_2, \quad \text{in } Q_T, && (2.10a)\\
-k(\theta)\frac{\partial\theta}{\partial\nu} &= \gamma(x,t)(\theta - \theta_\Gamma) \quad \text{in } \Sigma_T, && (2.10b)\\
\theta(.,0) &= \theta_0 \quad \text{in } \Omega. && (2.10c)
\end{aligned}$$

2.3 Heat source I: Laser radiation

Following the lines of Mazhukin and Samarskii [14], we assume that the laser radiation is absorbed volumetrically by the workpiece, acting as a thermal source of equivalent power. Let the part of the workpiece surface to be hardened lie in the plane $z = 0$ and suppose the laser beam strikes it in the point $(x_0, y_0) \in \partial\Omega$.
Then, the laser radiation penetrates into the workpiece according to the radiation transfer equation

$$\frac{\partial G}{\partial z} = \kappa G, \tag{2.11a}$$

$$G\Big|_{z=0} = \alpha G_f. \tag{2.11b}$$

Here, G is the radiation intensity of the laser beam, G_f the radiation intensity in the focal plane, κ the absorption coefficient and α the absorptivity of the surface, depending on the angle of incidence, the surface constitution (smoothness, cleanliness) and on the temperature.
For constant κ, we have

$$G = \alpha G_f e^{\kappa z}, \qquad z \leq 0. \tag{2.12}$$

G_f is supposed to satisfy a normal distribution law

$$G_f = G_0 e^{-\frac{(x-x_0)^2+(y-y_0)^2}{2R^2}},$$

where R is the radius of the focusing spot and G_0 its intensity in the spot center, i.e.

$$G_0 = P/\pi R^2, \tag{2.13}$$

with the radiation power P.
In applications, the laser beam moves along the workpiece surface according to a curve $t \longrightarrow r(t) \in \mathbb{R}^2$, $t \in [0, T]$, hence we have

$$G_f(x, y, t) = G_0 e^{-\frac{(x-r_1(t))^2+(y-r_2(t))^2}{2R^2}}.$$

The heat source in the case of laser hardening then takes the form

$$F_2 = \kappa G. \tag{2.14}$$

2.4 Heat source II: Induction heating

For the sake of simplicity, we assume that the workpiece is translational invariant in the direction of the z–axis with cross section $\Omega \subset \mathbb{R}^2$. In this geometric configuration, it

is reasonable to expect that the magnetic field has the form $\vec{H} = (0, 0, h)^T$. Neglecting displacement currents, Maxwell's equations then can be reduced to the following nonlinear parabolic equation (cf. e.g. [3]):

$$(\mu h)_t - \nabla.\Big(\frac{1}{\sigma(\theta)}\nabla h\Big) = 0, \quad \text{in } Q_T. \tag{2.15a}$$

Here, μ is the magnetic permeability and σ is the electric conductivity. Outside the conductors, h is constant, hence we consider a space–independent Dirichlet boundary conditon

$$h(.,t) = \varphi(t), \quad \text{in } \Sigma_T, \tag{2.15b}$$

and the initial condition

$$h(.,0) = h_0, \quad \text{in } \Omega. \tag{2.15c}$$

Owing to the Joule effect, the eddy currents induced in the workpiece act as a heat source, which can be described by

$$F_2 = \frac{1}{\sigma(\theta)}\Big|\nabla h\Big|^2. \tag{2.16}$$

2.5 Summary

The two models for surface hardening under study in this paper correspond to the following sets of equations:

a) Laser hardening **(LH)**

The model for laser hardening consists of the energy balance (2.10a–c), coupled with the system (2.7a–e) to describe the evolution of the phase fractions and the radiation transfer equation (2.11a,b).

b) Induction hardening **(IH)**

Here, the energy balance (2.10a–c) and the system (2.7a–f) have to be coupled with Maxwell's equations (2.15a–c).

Well–posedness of the model for laser hardening **(LH)** can be concluded from Theorem 3.1 in [9]. Existence and uniqueness for **(IH)** can be proved using a straightforward fixed point argument using Theorem 3.1 in [9] and Theorem 3.1 in [16].
To maintain the quality of the workpiece surface, it is very important to avoid melting effects. Especially in the case of laser hardening, which is often applied to curved edges, it is a delicate problem to obtain parameters that avoid melting but nevertheless lead to the desired hardening depth.

Mathematically speaking, this corresponds to minimizing the following cost functional

$$J = \int_\Omega \Big(z_4(x,T) - \tilde{m}(x)\Big)^2 dx,$$

subject to the state constraint $\theta \leq \theta_m$ and the state equations **(LH)**. Here, θ_m is the melting temperature and $\tilde{m}$ the desired distribution of martensite.
This control problem has been investigated in [11].

3 Numerical algorithm

To allow for variable time–step sizes, we introduce the following notations:
Let $M \in \mathbb{N}$ be fixed, $0 = t_0 < t_1 < \ldots < t_M = T$ be a partition of $[0,T]$ and

$$k_m = t_m - t_{m-1}, \qquad 1 \leq m \leq M.$$

Now, we introduce a time–discrete version of the system equations for **(LH)** and **(IH)**, respectively. We start with approximating the energy balance (2.10a–c): Let $\theta^m : \Omega \longrightarrow \mathbb{R}$ be the solution to

$$\begin{aligned} \rho(\theta^m)c(\theta^m)\frac{\theta^m - \theta^{m-1}}{k_m} + F_{11}(\theta^m, z^{m-1})A\left(\frac{\theta^m - \theta^{m-1}}{k_m}\right) & \\ -\nabla.\Big(k(\theta^m)\nabla\theta^m\Big) &= F_{12}(\theta^m, z^{m-1}) + F_2^m, \quad \text{in } \Omega \qquad (3.1a) \\ -k(\theta^m)\frac{\partial\theta^m}{\partial\nu} &= \gamma(\theta^m - \theta_\Gamma), \quad \text{in } \partial\Omega, \qquad (3.1b) \end{aligned}$$

for $1 \leq m \leq M$ and $\theta^0 := \theta_0$. Here, z^m is an approximation of $z(t^m)$, obtained from a fourth order Runge–Kutta method.
In the case of laser hardening, the heat source is discretized by

$$F_2^m = \frac{\kappa}{k_m}\int_{t_{m-1}}^{t_m} G dt.$$

In the case of induction hardening, the situation is more complicated. We have to cope with a rapidly oscillating magnetic field. Hence, φ in (2.15b) takes the form

$$\varphi(t) = \bar{h}\sin 2\pi\omega t, \qquad (3.2)$$

with frequencies ω between 10^4 and $10^6\, Hz$.
Therefore, as in [1], [3] or [12], we adopt the method of averaging. To this end, we introduce a new time–step size

$$\xi_m = \frac{k_m}{\omega N}, \quad N \in \mathbb{N} \text{ fixed},$$

where $1/\omega$ is the oscillation period in (3.2). Each time interval $[t_{m-1}, t_m]$ is dissected into $\omega \cdot N$ sub–intervals $[t_m^{j-1}, t_m^j]$ of length ξ_m, i.e. $t_m^j = t_{m-1} + j\xi_m$. Then, we consider the following time–discrete version of (2.15a-c):

$$\mu \frac{h_m^j - h_m^{j-1}}{\xi_m} - \nabla \left(\frac{1}{\sigma(\theta^{m-1})} \nabla h_m^j \right) = 0, \quad \text{in } \Omega, \tag{3.3a}$$

$$h_m^j = \bar{h} \sin(2\pi\omega t_m^j), \quad \text{in } \partial\Omega, \tag{3.3b}$$

for $1 \leq j \leq N$ and $h_m^0 := h_{m-1}$. The system (3.3a,b) is solved until the difference between the averaged gradient of the solution in two consecutive periods becomes small enough (cf. Fig. 11). The new value h_m is then obtained by averaging over the last period, and the heat source is given by

$$F_2^m = \frac{1}{\sigma(\theta^m)} \left| \nabla h^m \right|^2 . \tag{3.4}$$

The space discretizations of both the nonlinear heat conduction problem and the Maxwell equation are carried out with a Voronoi box based vertex centered finite volume method on one–, two– and three–dimensional simplicial meshes. Mesh generation is performed using the grid generator IBG [17].

The solution of the discrete nonlinear heat conduction problem is obtained using Newton-Krylov methods.

When coupled with the time–step control in the right way, Newton's method shows quadratic convergence behaviour, which makes it possible to obtain very exact solutions to the nonlinear problems at low additional cost.

The solution of the linear problems uses the method of conjugated gradients for the Maxwell equation and the BICGstab method for the linear problems occuring during the Newton process in the heat conduction equation, respectively. These methods are preconditioned by incomplete LU factorizations. On rectangular meshes, efficient multigrid preconditioners can be used as well. The development of multigrid preconditioners for unstructured meshes is still going on (cf. [6]).

A more thorough description of the nonlinear solution methods can be found in [7], where these methods are applied to a nonlinear porous media flow problem with a structure very similar to the nonlinear heat conduction problem under study in this paper.

4 Simulations for the steel 42 CrMo 4

4.1 Physical data

The numerical simulations are carried out for the steel 42 CrMo 4. Table 1 depicts its chemical composition. The temperature–dependent coefficients ρ, c, k have been taken

C	Si	Mn	P	S	Cr	Cu	Mo	Ni
0.38	0.23	0.64	0.019	0.013	0.99	0.17	0.16	0.08

Table 1: Chemical composition of the steel 42 CrMo 4 (from [13]).

from [4]. Here and in the sequel we use cubic splines to interpolate between values for different temperatures in order to obtain convergence of the Newton algorithm.
We use (2.6a,b) to describe the formation of austenite during heating. The values for the temperature–dependent coefficients a_{eq} and τ have been taken from [15]. For A_s we use the value

$$A_s = 730\,^oC.$$

According to Fig. 3, during cooling four phase transitions may occur. However, in the case of surface hardening we encounter high cooling rates. Hence, it is sufficient to restrict ourselves to the formation of bainite and martensite. The kinetics of these phase transitions can be drawn from the isothermal *time–temperature–transformation diagram* depicted in Fig. 4.
For the formation of bainite we make the ansatz

$$b_t = f(b)\,g(\theta), \tag{4.1}$$

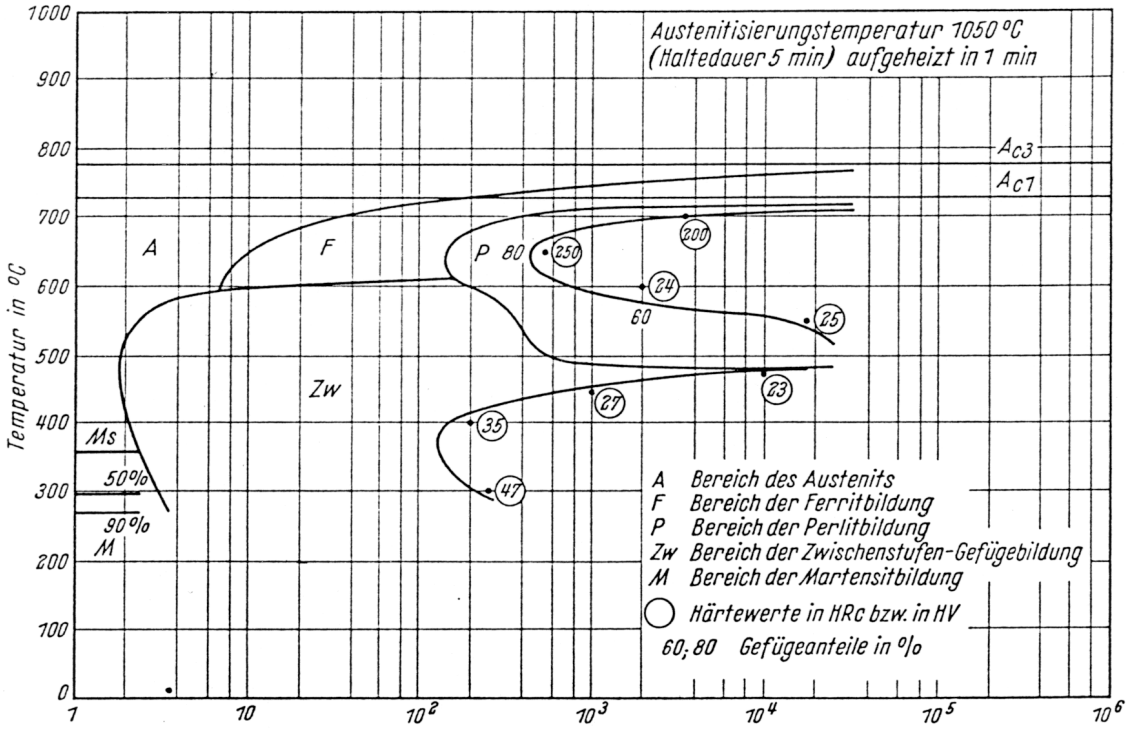

Figure 4: Isothermal time–temperature–transformation diagram for the steel 42CrMo4 (from [13]).

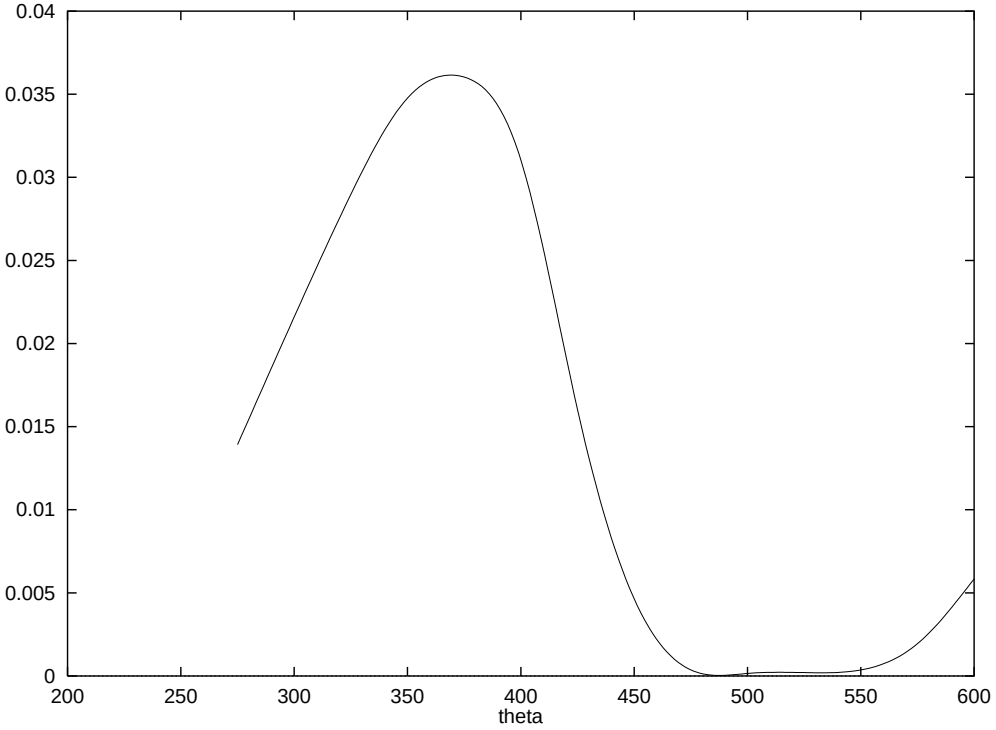

Figure 5: Graph of the function $g(\theta)$ in (4.4).

where b is the volume fraction of bainite (cf. Sec. 2.1).
For fixed temperature θ, the curved lines in Fig. 4 denote the beginning (t_s) and the end (t_f) of transformation, defined by volume fractions $b = 0.01$ and $b = 0.99$, respectively. Integrating (4.1) keeping θ fixed, we obtain

$$g(\theta) = \frac{1}{t_f - t_s} \int_{0.01}^{0.99} \frac{1}{f(b)} db. \tag{4.2}$$

A frequently used ansatz for f is

$$f(b) = b^q (1-b)^{1-q}, \qquad \text{and } q \in [0,1]. \tag{4.3}$$

Another approach, using the Johnson–Mehl equation, can be found in [10]. Choosing $q = 0$ in (4.3), we obtain

$$g(\theta) = \frac{1}{t_f - t_s} \ln(99)\,. \tag{4.4}$$

The values for t_f and t_s can be drawn from Fig. 4. Figure 5 shows the graph of $g(\theta)$.
For the formation of martensite we use the ansatz

$$m_t = (1-m)\, c_m\, \mathcal{H}(-\theta_t)\, \mathcal{H}(M_s - \theta). \tag{4.5}$$

The constants c_m and M_s can be identified from the volume fractions of martensite depicted in Fig.4. We chose

$$c_m = 1.4, \qquad M_s = 360^\circ C. \tag{4.6}$$

description	denotation	value (range)	unit
radius of focusing spot	R	0.25, ...,0.9	cm
radiation power	P	2000	W
absorption coefficient	κ	4.0	$1/cm$
absorptivity	α	37.5	
laser beam velocity	v	50, ...,150	cm/s
scanning width	s	0.0, ..., 1.3	cm
frequency of oscillation	f	175	Hz

Table 2: Physical data for laser hardening.

Replacing $1-b$ and $1-m$ with the actual volume fraction of austenite, we end up with the following initial–value problem:

$$a(0) = b(0) = m(0) = 0, \tag{4.7a}$$

$$a_t(t) = \frac{1}{\tau(\theta(t))} \max\left\{a_{eq}(\theta(t)) - a(t)\,,\, 0\right\} \mathcal{H}(\theta - A_s) - b_t(t) - m_t(t), \tag{4.7b}$$

$$b_t(t) = a(t)\, g(\theta(t)), \tag{4.7c}$$

$$m_t(t) = a(t)\, c_m \mathcal{H}(-\theta_t(t)) \mathcal{H}(M_s - \theta(t)). \tag{4.7d}$$

In our simulations we assume further that the latent heat L is the same for all the phase transitions, namely

$$L = 82 \left[\frac{\mathrm{J}}{\mathrm{g}}\right]. \tag{4.8}$$

Then, the functions F_{11} and F_{12} in (2.9b,c) take the form

$$F_{11}(\theta, a, b, m) = \rho(\theta)\, L\, c_m\, a\, \mathcal{H}(M_s - \theta), \tag{4.9}$$

$$F_{12}(\theta, a, b, m) = -\frac{\rho(\theta)\, L}{\tau(\theta)} \max\left\{a_{eq}(\theta) - a\,,\, 0\right\} \mathcal{H}(\theta - A_s) + \rho(\theta)\, L\, a\, g(\theta). \tag{4.10}$$

4.2 Numerical results for laser hardening

A disadvantage of laser hardening is that no additional spray water cooling can be applied to support the quenching process. This is reflected in numerical simulations: To obtain the desired hardening effect by the formation of martensite, one has to make full 3–d calculations, otherwise not enough heat can be carried off.

We simulate the hardening along a strip around the y–axis on the upper face ($z = 0$) of the cube $\bar{\Omega} = [-2.5, 2.5] \times [0, 10.0] \times [-1.0, 0]$. The values for the physical parameters used in these calculations can be found in Table 2. They correspond to a 2.8 kW Nd:YAG–laser.

Since the main quenching effect is the self–cooling of the workpiece, we assume $\gamma \equiv 0$ in (3.1b), i.e. a homogenous Neumann boundary condition for θ.

The scanning width s is twice the amplitude of the oscillations orthogonally to the moving direction related to the spotcenter, and f their frequency. The remaining parameters are explained in Sec. 2.3. The absorption coefficient κ and the absorptivity α have been gauged by comparison with measured hardening profiles.

Figure 6 shows the time evolution at the point $x = (0.0, 1.0, -0.01) \in \Omega$. Owing to the oscillations of the laser beam, the point is heated by steps. Austenite is formed, and during cooling this austenite is transformed to martensite and a fairly small amount of bainite. In the course of martensite growth, the cooling process is slowed down by the release of latent heat.

Figure 7 depicts the temperature distribution on the upper surface of Ω at time $t = 3\,s$. The variety of possible hardening profiles and the interplay between the control parameters R and v is illustrated in Figs. 8 and 9. The profiles in Fig. 8 are obtained without oscillations of the laser beam. The widening of the hardness profile has been achieved by increasing the radius R of the focusing spot. Since increasing R leads to a decrease of the radiation intensity G_0 (cf. (2.13)), the velocity has to be reduced in order to get the same depth of the hardening profile.

In Fig. 9, the spot radius is the same as in Fig. 8(a). Here, the widening of the profile has been achieved by letting the laser beam oscillate orthogonally to the moving direction. While the amplitude is the same in (a) and (b), the kind of oscillation is different. The

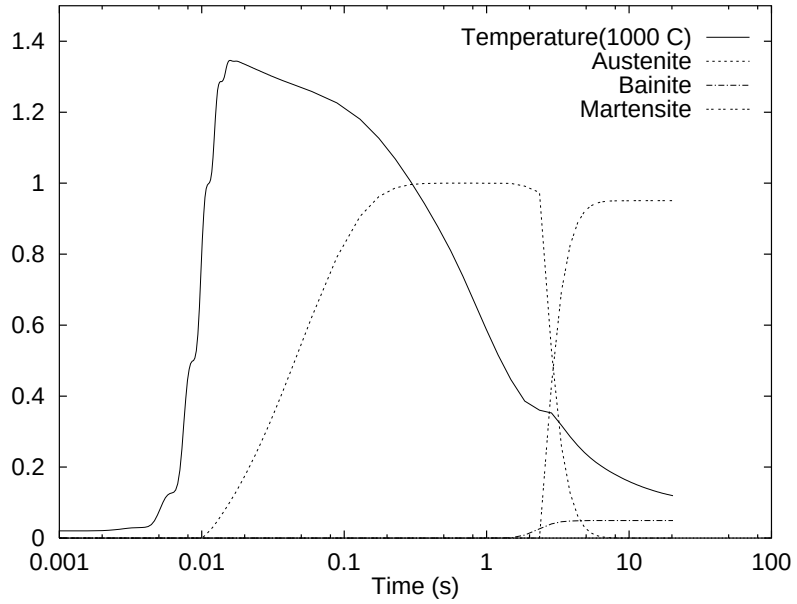

Figure 6: Time evolution of temperature, austenite, bainite and martensite fraction for $x = (0.0, 1.0, -0.01) \in \Omega$.

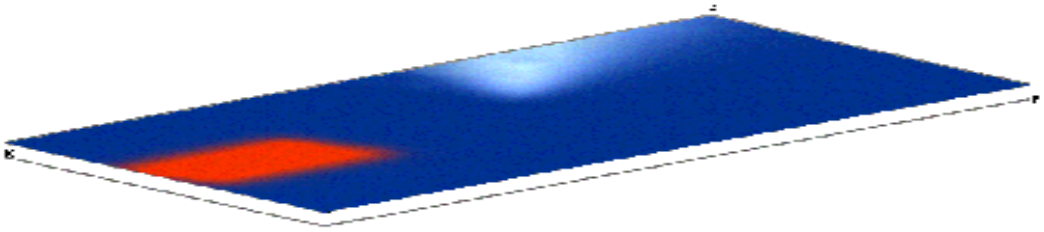

Figure 7: Temperature distribution on the upper workpiece surface at time $t = 3.0s$.

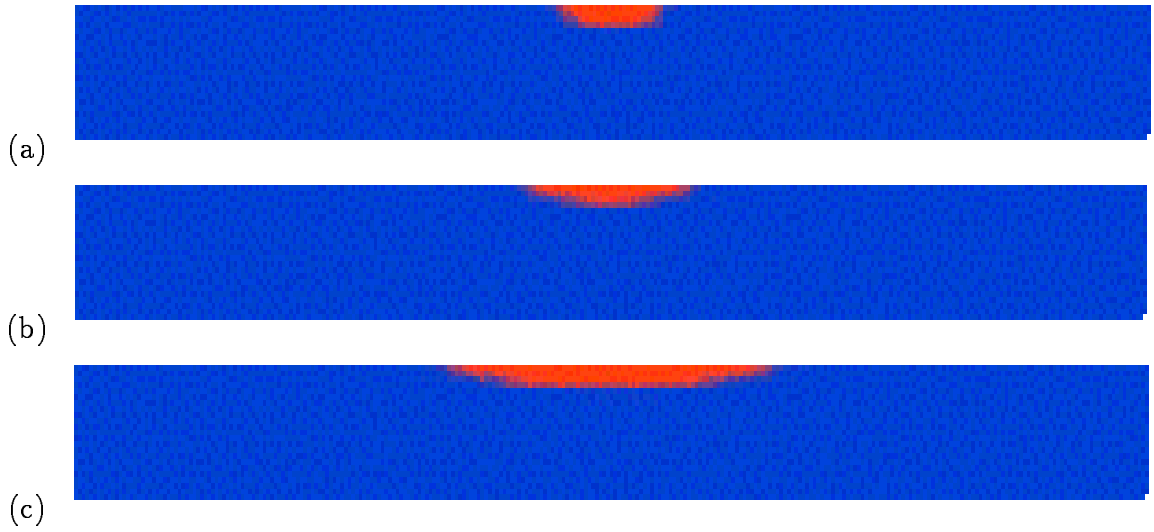

Figure 8: Hardening profile at $y = 1.0$, no oszillations; (a) $R = 0.25\,cm$, $v = 150\,cm/s$; (b) $R = 0.5\,cm$, $v = 50\,cm/s$; (c); $R = 0.9\,cm$, $v = 50\,cm/s$.

Figure 9: Hardening profile at $y = 1.0$; (a) sawtooth oscillations, $R = 0.25\,cm$, $s = 1.3\,cm$, $v = 100\,cm/s$; (b) sinusoidal oscillations, $R = 0.25\,cm$, $s = 1.3\,cm$, $v = 80\,cm/s$.

sawtooth form in Fig. 9(a) leads to a uniform heating along the hardening strip, while the sinusoidal oscillations in Fig. 9(b) preferentially heat the boundary of the strip. This leads to a further widening of the hardening profile, but to obtain the same profile depth as before, the velocity has to be reduced.

4.3 Numerical results for induction hardening

For the magnetic permeability we use the value

$$\mu = 4\pi \cdot 10^{-9} \quad \frac{V\,s}{A\,cm}.$$

The electric conductivity is assumed to be temperature–dependent, i.e.

$$\sigma(\theta) = \frac{1}{c_1 + c_2\theta + c_3\theta^2 + c_4\theta^3} \quad \frac{1}{\Omega\,cm},$$

with $c_1 = 4.9656 \cdot 10^{-5}$, $c_2 = 8.4121 \cdot 10^{-8}$, $c_3 = -3.7246 \cdot 10^{-11}$, $c_4 = 6.1960 \cdot 10^{-15}$ (cf. [3]).

We call t_1 the time, until when the workpiece is heated by the eddy currents, and assume that the water cooling starts at t_1. Hence, the Dirichlet condition in (2.15b) takes the form

$$\varphi(t) = \begin{cases} \bar{h}\sin(2\pi\omega t), & 0 \le t < t_1, \\ 0, & t \ge t_1, \end{cases} \tag{4.11}$$

with $\bar{h} = 1.5 \cdot 10^3\, A/cm$. The heat exchange coefficient γ in (2.10b) has been chosen according to [10] as

$$\gamma(t) = \begin{cases} 0, & 0 \le t < t_1, \\ 2.8, & t \ge t_1, \end{cases}$$

expressed in $J/cm^2\,s\,K$. We simulate the surface hardening of a 'very thick' gear–wheel. For symmetry reasons, the domain can be reduced to the sector Ω depicted in Fig. 10.

As explained in Sec. 3, we have to work with two time–scales. In each time–step k_m we solve (3.3a,b), until the difference between the averaged gradient of the solution in two consecutive periods becomes small enough (see Fig. 11).

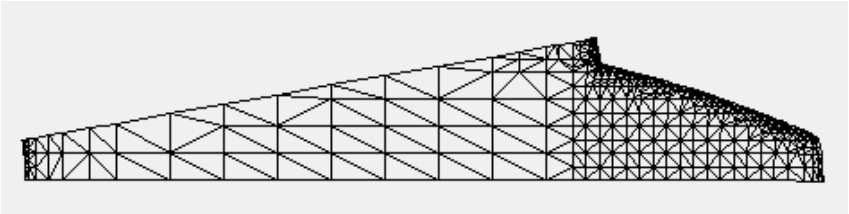

Figure 10: Computational domain.

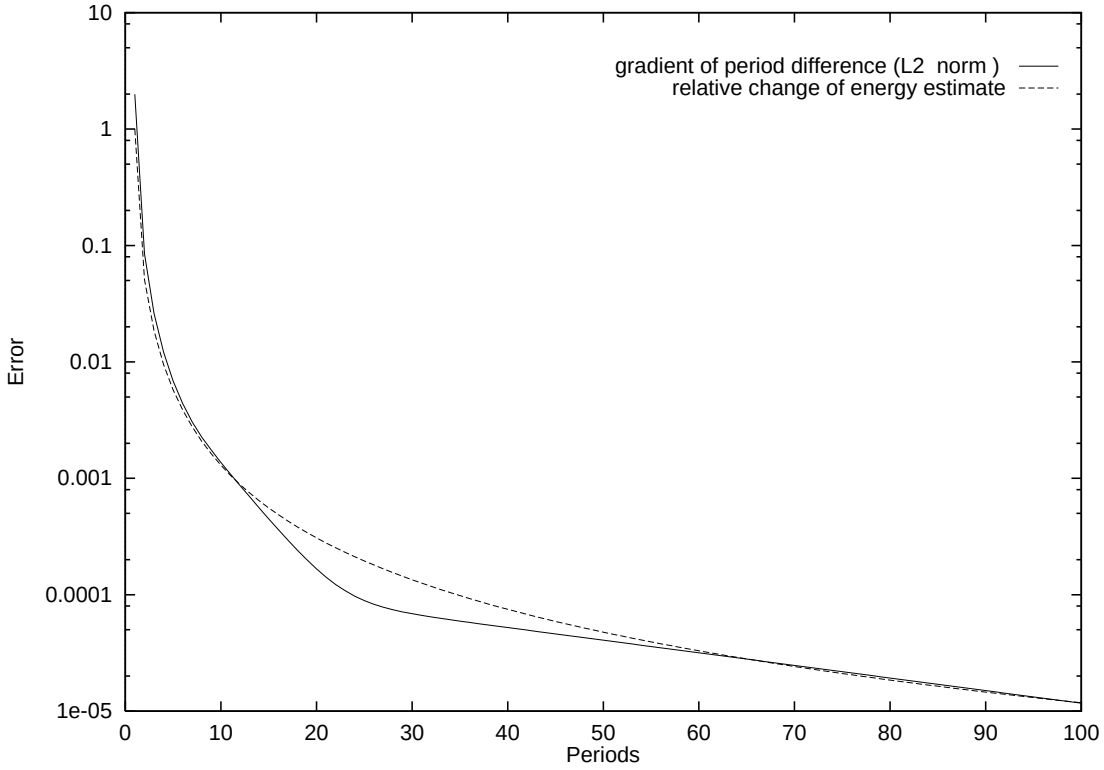

Figure 11: Difference between the averaged gradient of the solution in two consecutive periods in different norms and relative change of energy estimate, θ fixed.

In two space dimensions, the magnetic field is constant outside Ω. Therefore, geometric effects like a varying distance between the workpiece Ω and the coil (cf. Fig. 1) cannot be taken into account. Thus, the important control parameters in our simulations are the frequency ω and the heating time t_1.
Figure 12 depicts the result of a simulation at time $t = 0.42\,s$. The left gear–wheel shows the temperature distribution while the right one represents the distribution of phases.
Figure 13 shows the influence of the skin effect on the hardening depth. With growing frequency, the hardening depth decreases.
These are only qualitative results. To obtain quantitative predictions, the amplitude $\bar{h}$ in (4.11), which we have estimated numerically in order to get visible hardening depths, has to be gauged by comparison with experiments.

5 Conclusions

We have investigated a mathematical model for laser and induction surface hardening, including the occuring phase transitions that produce the hardening effect. In the simulations presented here, the formation of bainite is negligible (always less than 5%). However, if workpieces with more complicated geometries are considered, where the heat cannot be

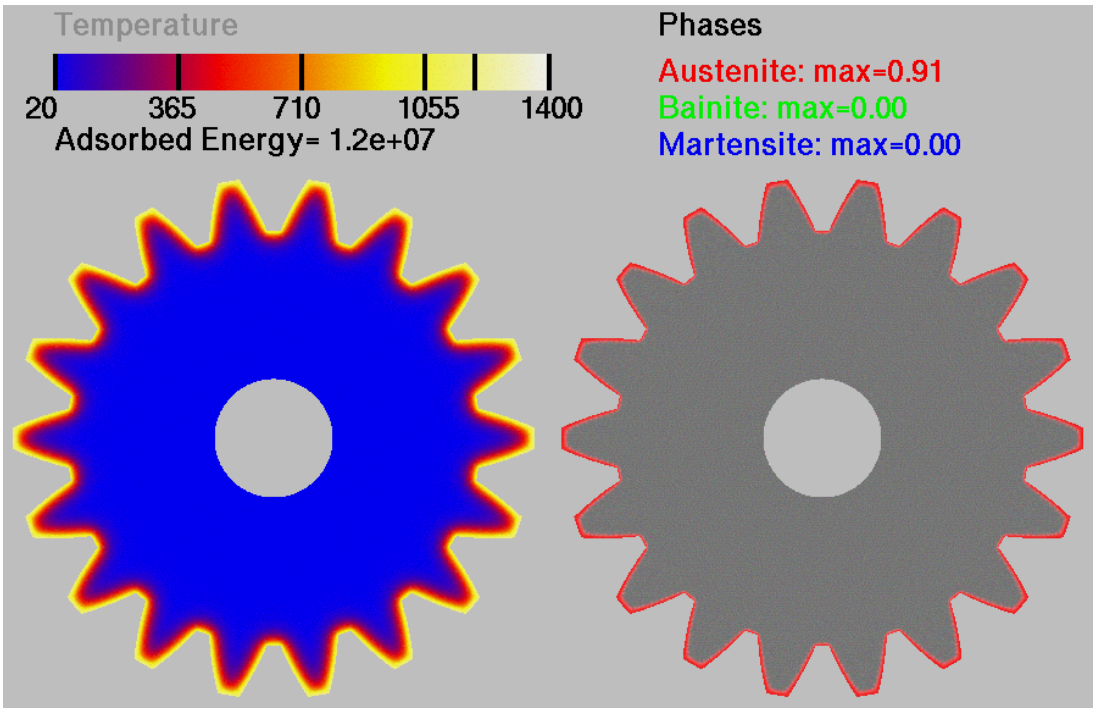

Figure 12: Result of the numerical simulation at time $t = 0.42\,s$, $t_1 = 0.48\,s$, $\omega = 10^5\,Hz$.

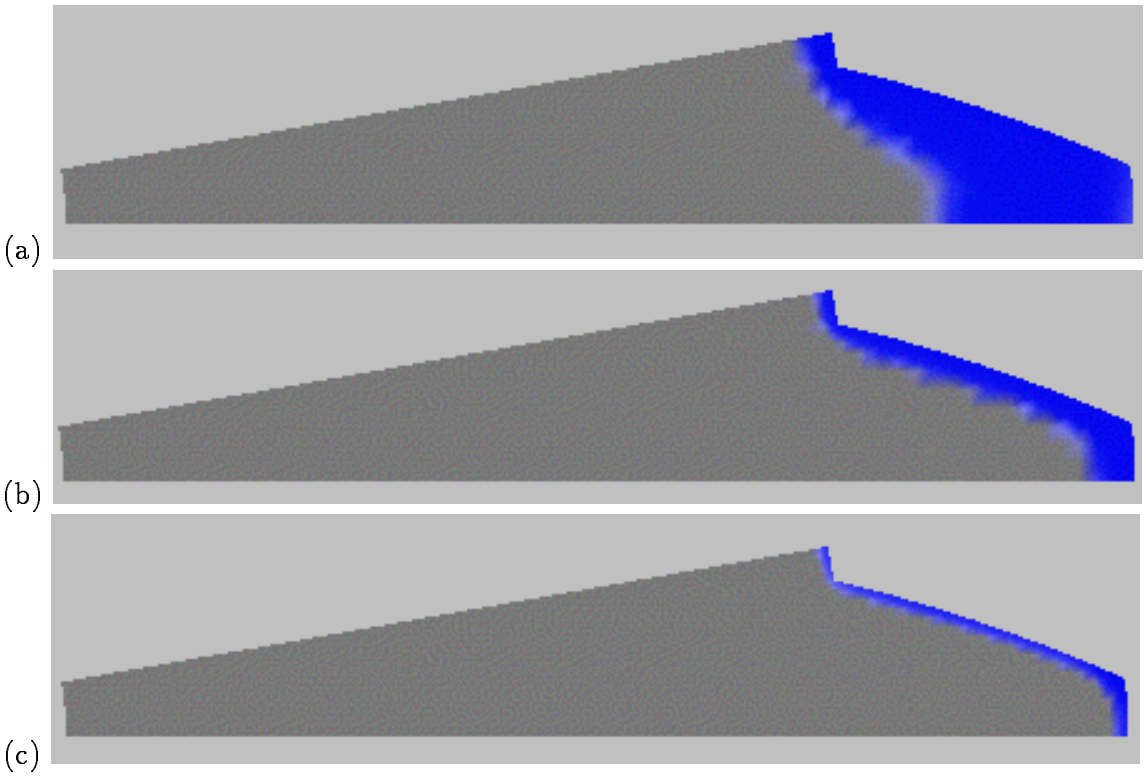

Figure 13: Influence of the skin effect on the hardening depth: (a) $\omega = 10^4\,Hz$, $t_1 = 3.3\,s$; (b) $\omega = 10^5\,Hz$, $t_1 = 0.48\,s$; (c) $\omega = 10^6\,Hz$, $t_1 = 0.06\,s$.

carried off fast enough, the growth of bainite becomes important.
Concerning laser hardening, a comparison between Figures 8 and 9 shows that instead of simply increasing the spot radius, the widening of a hardness profile can be achieved more efficiently, if the beam oscillates orthogonally to the moving direction.
For more complex geometries, the estimation of parameters for laser hardening is a difficult task. Hence, an important direction for further research is the development of numerical optimization strategies.
In the case of induction hardening, the numerical results show all the features that are observed in practice. However, a very important practical issue with a huge demand for numerical simulations is the design of optimal coils for workpieces with complicated geometries. This problem cannot be treated in the 2D approximation of Maxwell's equations considered here, since in this case the magnetic field is space–independent outside the workpiece making it impossible to account for a varying distance between workpiece and coil.
Therefore, the development of efficient solvers for Maxwell's equations in three space–dimensions is another important direction of further research.

References

[1] Bossavit, A., *Free boundaries in induction heating*, Control Cybern., 14, (1985), 69–96.

[2] Bossavit, A., Rodrigues, J.–F., *On the electromagnetic "Induction Heating" Problem in bounded domains*, Adv. Math. Sc. Appl., 4, (1994), 79–92.

[3] Clain, S. et al., *Numerical modelling of induction heating for two–dimensional geometries*, Math. Models Methods Appl. Sci., Vol. 3, No. 6 (1993), 271–281.

[4] Energie– und Betriebswirtschaftsstelle des Vereins Deutscher Eisenhüttenleute, *Anhaltszahlen für die Wärmewirtschaft in Eisenhüttenwerken*, Verlag Stahleisen mbH, Düsseldorf, 1968.

[5] Fasano, A., Primicerio, M., *An analysis of phase transition models*, European J. Appl. Math., 7, (1996), 439–451.

[6] Fuhrmann, J., *On numerical solution methods for nonlinear parabolic problems*, Proceedings of the 1st GAMM-Seminar on Modelling and Computation in Environmental Sciences Stuttgart, 12.-13.10.1995, to appear in Notes Numer. Fluid Mech.

[7] Fuhrmann, J., *Outlines of a modular algebraic multigrid method*, in: Proceedings of the Conference on Algebraic Multilevel Iteration Methods, Nijmegen, 13.-15.6.1996, eds. O. Axelsson and B. Polman, Nijmegen, 1996.

[8] Hömberg, D., *A mathematical model for the phase transitions in eutectoid carbon steel*, IMA J. Appl. Math., 54 (1995), 31–57.

[9] Hömberg, D., *Irreversible phase transitions in steel*, Math. Methods Appl. Sci., 20, (1997), 59–77.

[10] Hömberg, D., *A numerical simulation of the Jominy end–quench test*, Acta Mater., 44, (1996), 4375–4385.

[11] Hömberg, D., Sokolowski, J., *Optimal control of laser hardening*, Adv. Math. Sci. Appl., to appear.

[12] Hoppe, R.H.W., Kornhuber, R., *Multi–grid solution of two coupled Stefan equations arising in induction heating of large steel slabs*, Internat. J. Numer. Methods Engrg., 30, (1990), 779–801.

[13] Max–Planck–Institut für Eisenforschung und der Werkstoffausschuss des Vereins Deutscher Eisenhüttenleute, *Atlas zur Wärmebehandlung der Stähle, Teil I+II*, Verlag Stahleisen mbH, Düsseldorf, 1961.

[14] Mazhukin, V.I., Samarskii, A.A., *Mathematical modeling in the technology of laser treatments of materials*, Surveys Math. Indust. **4** (1994) 85–149.

[15] Leblond, J.–B., Devaux, J., *A new kinetic model for anisothermal metallurgical transformations in steels including effect of austenite grain size*, Acta Met. 32, (1984), 137–146.

[16] Rodrigues, J.–F., *A nonlinear parabolic system arising in thermomechanics and in thermomagnetism*, Math. Models Methods Appl. Sci., 2, (1992), 271–281.

[17] Schmelzer, I., *3D anisotropic grid generation with intersection-based geometry interface*, IMA preprint series no. 1180, 1993.

[18] Tiba, D., Neittaanmaki, P., *Optimal control of nonlinear parabolic systems*, Monographs Textbooks Pure Appl. Math. 179, M. Dekker, New York, 1994.

[19] Verdi, C., Visintin, A., *A mathematical model of the austenite-pearlite transformation in plain steel based on the Scheil's additivity rule*, Acta Metall., 35, No.11 (1987), 2711–2717.

[20] Visintin, A., *Mathematical models of solid–solid phase transitions in steel*, IMA J. Appl. Math., 39 (1987), 143–157.

List of Figures

List of Tables